The Response of the Near-Surface Tropical Cyclone Wind Field to Inland Surface Roughness Length and Soil Moisture Content during and after Landfall

JAMES HLYWIAK[a] AND DAVID S. NOLAN[a]

[a] *Rosenstiel School of Marine and Atmospheric Sciences, University of Miami, Miami, Florida*

(Manuscript received 9 July 2020, in final form 15 November 2020)

ABSTRACT: The sensitivity of the inland wind decay to realistic inland surface roughness lengths and soil moisture contents is evaluated for strong, idealized tropical cyclones (TCs) of category 4 strength making landfall. Results show that the relative sensitivities to roughness and moisture differ throughout the decay process, and are dependent on the strength and size of the vortex. First, within 12 h of landfall, intense winds at the surface decay rapidly in reaction to the sudden change in surface roughness and decreasing enthalpy fluxes. Wind speeds above the boundary layer decay at a slower rate. Differences in soil moisture contents minimally affect intensity during the first 12 h, as the enhancement of latent heat fluxes from high moisture contents is countered by enhanced surface cooling. After TCs decay to tropical storm intensities, weakening slows and the sensitivity of the intensity decay to soil moisture increases. Increased latent heating becomes significant enough to combat surface temperature cooling, resulting in enhanced convection outside of the expanding radius of maximum winds. This supports a slower decay. Additionally, the decay of the radial wind profile by quadrant is highly asymmetric, as the rear and left-of-motion quadrants decay the fastest. Increasing surface roughness accelerates the decay of the strongest winds, while increasing soil moisture slows the decay of the larger TC wind field. Results have implications for inland forecasting of TC winds and understanding the potential for damage.

KEYWORDS: Boundary layer; Hurricanes/typhoons; Numerical analysis/modeling

1. Introduction

Tropical cyclones (TC) nearly always undergo weakening upon landfall. After landfall, TCs become increasingly removed from high heat and moisture fluxes provided by the warm tropical ocean waters (Ooyama 1969; Marks et al. 1998). In addition, the drastically rougher land surface acts as a sink for momentum, reducing TC boundary layer (TCBL) winds (Miller 1964; Eliassen 1971; Montgomery et al. 2001; Chen and Chavas 2020). The former mechanism affects surface winds indirectly by modifying the core structure of the TC, while the latter directly reduces surface winds, weakening the TC from the bottom upward. Other important factors for weakening vary by location and depend on the state of the atmosphere, such as interactions with topography and extratropical systems (Bender et al. 1987; Yang et al. 2011; Evans et al. 2017; Leroux et al. 2018).

Even as a TC weakens, intense chaotic winds and inland flooding pose threats to society. Empirically derived inland decay models help improve global and statistical model forecasts and have aided in revealing dominant predictors of intensity decay such as intensity at landfall, TC translation speed, and atmospheric humidity (Kaplan and DeMaria 1995, hereafter KD95; Vickery 2005; Wong et al. 2008). By necessity, characteristics of the underlying surface are often oversimplified by this approach. Regardless, the fact that empirical decay functions differ between regions suggests that the intensity decay rate is sensitive to unique surface characteristics (Kaplan and Demaria 2001; DeMaria et al. 2006; Wong et al. 2008). Recent studies have revealed much about the surface wind and heat flux profiles over land partly thanks to improvements in wind sampling technologies within intense winds (Masters et al. 2010; Giammanco et al. 2012; Kosiba and Wurman 2014; Krupar et al. 2016; Alford et al. 2019, 2020). However, obtaining dense observations of the low-level wind field over land remains a challenging and risky endeavor, resulting in sparse observations and datasets.

A handful of idealized and case studies argue that the low thermal inertia—defined as the square root of the product of the thermal diffusivity and specific heat capacity—of soil is the principal cause for inland cyclone decay (Bender et al. 1987; Tuleya 1994, hereafter T94; Shen et al. 2002; Kishtawal et al. 2012). Inland thermal inertia is typically two orders of magnitudes lower than that over the oceans; thus, surface heat is depleted rapidly over land. T94 showed that TCs fail to intensify from weak vortices over surfaces characterized by low thermal inertia, while increasing thermal inertia beyond typical values for soil to that of the tropical oceans supports intensification. Additionally, T94 revealed that increasing surface roughness to a moderate value of 25 cm was shown to weaken the surface wind footprint of the storm while winds aloft were relatively unaffected. T94 concluded that the surface-based intensity is sensitive to the surface roughness; however, a storm in a high-friction environment may persist for a longer period of time over surfaces characterized by high thermal inertia. Shen et al. (2002) found that increasing soil roughness lengths from 1 to 10 cm increased the efficiency of the surface heat transfer. This suggests that the decrease of the surface winds due to the increase in roughness may be compensated to an extent by the strengthening of the vortex through enhanced surface heat fluxes.

Similarly, studies have linked abnormally high soil moisture to inland reintensification. Inland rejuvenation of low pressure systems occurs relatively frequently over the northern deserts

---

Corresponding author: James Hlywiak, jhlywiak@rsmas.miami.edu

DOI: 10.1175/JAS-D-20-0211.1

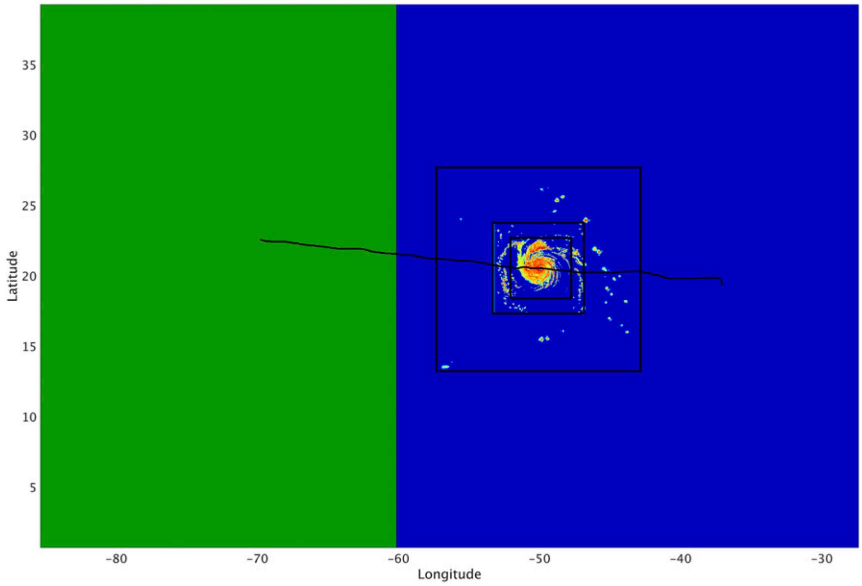

FIG. 1. Model-produced radar reflectivity field ($\lambda = 10$ cm) at the time of land initialization for moderate–moderate (MM), 3 days from the initialization of the ocean-only case, relative to the sizes of each domain and the location of land. The 8-day track is shown in black. Land (ocean) is in green (blue).

of Australia (Emanuel et al. 2008, hereafter E08; Andersen and Shepherd 2014; Tang et al. 2016; Kilroy et al. 2016b). E08 hypothesized that soil moistening due to rainfall ahead of a storm increases the thermal conductivity of the soils, resulting in more sustained latent heat fluxes. Kilroy et al. (2016b) and Tang et al. (2016) found similar results, contending that as long as deep convection persists near the core, horizontal transport of environmental moisture can balance the moisture lost to precipitation.

Tropical Storms Erin (2007) and Fay (2008) are two cases of observed inland TC intensification over the United States. These storms encountered warm land temperatures and saturated soils over Oklahoma and Florida, respectively, which are hypothesized to have aided in the strengthening of each cyclone (Evans et al. 2011; Kellner et al. 2012; Bozeman et al. 2012). In the case of Erin, Evans et al. (2011) discussed how seasonally above-average rainfall during the preceding months over Texas and Oklahoma contributed significantly to the moisture budget of the TC, while the rains produced by the TC itself had little impact on Erin.

However, the aforementioned cases are unique, and have only been observed for weak inland tropical storms and low pressure systems. Additionally, it is difficult to determine the contribution of surface effects to the TC structure from observations as the decay response inevitably varies due to atmospheric conditions as well. Thus, whether a range of realistic soil properties can slow the inland decay of a powerful storm is still unclear.

The main goal of this study is to evaluate the sensitivity of the near-surface wind decay within mature, landfalling idealized TCs to inland surface roughness and soil moisture content. We focus on the low-level winds, since this is where the highest impact on lives and property occurs. Our results show that the wind field decay is initially sensitive to the surface roughness within 12 h of landfall and beyond, and that the sensitivity to soil moisture contents increases farther inland after significant weakening and TC size expansion has occurred.

2. Methods

a. Model specifications and vortex initialization

The Advanced Research version of the Weather Research and Forecasting (WRF) (ARW) Model, version 3.9.1.1, was used for this study. All landfall simulations originated from an ocean-only simulation lasting 8 days. This ocean-only case was initialized from a weak vortex of tropical storm strength in a

TABLE 1. Set of roughness length (Z_0) and soil moisture (S_c) sensitivity tests.

	Z_0 (cm)		
S_c	5	25	50
0.6	Smooth + wet (SW)	Moderate + wet (MW)	Rough + wet (RW)
0.3	Smooth + moderate (SM)	Moderate + moderate (MM)	Rough + moderate (RM)
0.05	Smooth + dry (SD)	Moderate + dry (MD)	Rough + dry (RD)

TABLE 2. Soil heat capacity (C, $\times 10^6$ J m^{-3} K^{-1}), thermal diffusivity (K_t, J m^{-1} s^{-1} K^{-1}), and thermal inertia (I_q, $\times 10^3$ J m^{-2} K^{-1} s$^{-1/2}$) for each S_c value, fully saturated soil in our simulations, the soil and next driest cases in T94, and the values for dry and wet sand used in E08.

	0.05	0.3	0.6	1.0	T94 soil	T94 dry	E08 dry	E08 wet
C	0.211	1.26	2.52	4.20	—	—	1.28	3.36
K_t	0.17	2.84	13.8	79.5	—	—	0.358	3.36
I_q	0.192	1.89	5.90	18.27	2.09	13.3	0.677	3.36

mean easterly flow following the point-downscaling method described in Nolan (2011). Environmental winds decreased sinusoidally from 6.5 m s^{-1} at 850 hPa to 1 m s^{-1} at 200 hPa, resulting in 5.5 m s^{-1} of westerly shear [refer to Fig. 2 of Onderlinde and Nolan (2017) for an example of a similar profile]. The atmosphere was initialized with the Jordan mean sounding (Jordan 1958). We chose to use this sounding instead of the commonly used Dunion moist sounding (Dunion 2011) because the drier Jordan sounding better reflects a blend of tropical maritime and continental air masses. Additional experiments using the Dunion moist sounding produced TCs that were larger in area and marginally more intense; however, our

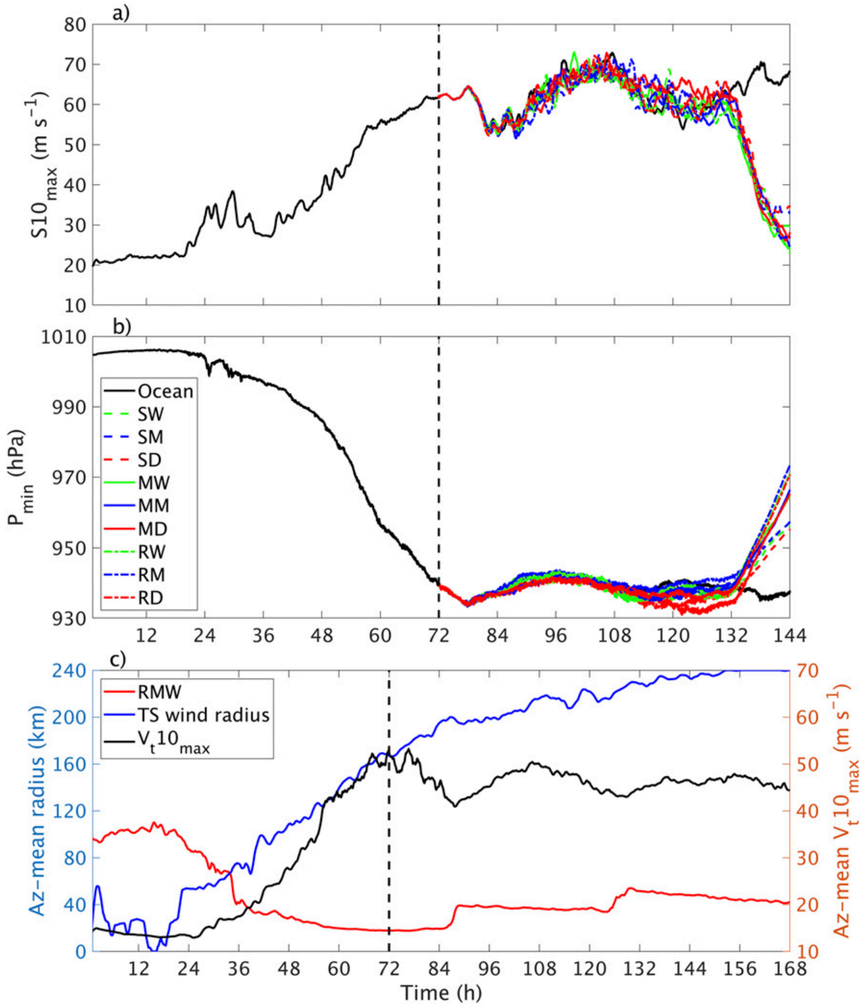

FIG. 2. (a) Maximum 10 m wind speed ($S10_{\max}$; in m s^{-1}), with a 1 h running mean applied; (b) minimum surface pressure ($P_{\min}$; in hPa); (c) left axis: RMW (red) and radius of TS-force winds (blue) for the ocean-only case; right axis: azimuthally averaged 10 m tangential wind maximum for the ocean-only case. The x axis shows time since the initialization of the ocean-only simulation. Note the longer time frame in (c). The initialization time of the landfall cases at 72 h is shown in the black vertical dashed line.

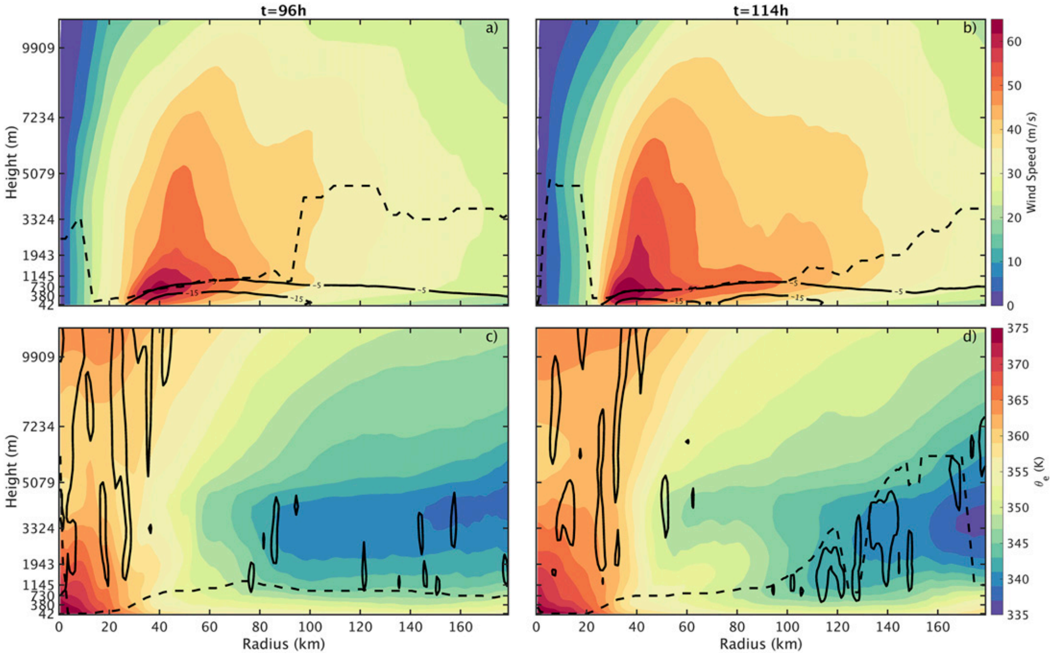

FIG. 3. (a),(b) Azimuthally averaged tangential (colored contours) and radial (solid black contours at −5 and $-15\,\mathrm{m\,s^{-1}}$) winds for the ocean-only case as a function of radius at 96 and 114 h after the start of the simulation, respectively. The TCBL height defined as the height of maximum tangential wind speed is plotted by the dashed black line. (c),(d) Azimuthally averaged θ_e (colored contours) and negative vertical velocity (solid black contours of $-0.1\,\mathrm{m\,s^{-1}}$) for the ocean-only case at the same two times. The TCBL height defined as the depth of the inflow (see section 3b) is plotted by the dashed black line. The y-axis tick marks are placed every fourth unstaggered vertical level, starting with the lowest model level.

main results did not noticeably differ otherwise (not shown). The 1D mixed layer model within WRF (Pollard et al. 1972) was used to simulate the ocean, which was initially quiescent and featured sea surface temperatures of 28°C above a mixed layer depth of 50 m. Ocean temperature and density were initially horizontally homogeneous at each depth. Landfall simulations were initialized by pausing the ocean case after 72 h and restarting with an idealized landmass over the western portion of the domain (Fig. 1). Landfalling TCs then translated over an additional 5 days toward the west with a slight poleward drift as the TC intensified. The coastline was placed roughly 1100 km from the TC center, which was defined as the centroid of the pressure field, similar to Nguyen et al. (2014). We define landfall as when the center crosses the coastline. Landfall occurred about 60 h after restarting, resulting in a consistent translation speed around $5.5\,\mathrm{m\,s^{-1}}$, a value typical of many TCs that make landfall in the Atlantic basin (Yablonsky and Ginis 2009; Kossin 2018). The TC translation speed has been shown to affect inland wind penetration (KD95); however, for simplicity we chose to evaluate a common landfall speed.

Three nested, vortex-following grids of $\delta x = 9$, 3, and 1 km, and $\delta t = 45$, 15, and 5 s spanning 180 × 180, 240 × 240, and 480 × 480 grid points were embedded within a doubly periodic parent domain of $\delta x = 27$ km, $\delta t = 90$ s, and 240 × 160 grid points in the zonal and meridional directions. Simulations were performed on an f plane with the Coriolis parameter set to a value corresponding to 20°N. Large-scale nudging of the atmospheric environmental winds, specific humidity, and temperature was applied to only the outermost domain following the methods outlined in Onderlinde and Nolan (2017) using a relaxation time-scale $\tau = 24$ h. Nudging was deactivated below 2 km. Restricting the nudging to the outermost domain permitted the immediate environment of the cyclone to evolve with minimal influence from the large-scale environment, while ensuring that the large-scale steering-flow remained constant. Figure 1 shows the relative size of one of the landfall TCs at the time the land was initialized with the 8-day track. The atmosphere consisted of 50 vertical mass levels, with 17 of these levels concentrated below 2 km. Output variables at the surface and the model diagnosed 10 m wind speeds within the innermost domain were stored every 30 s. Above this, variables were recorded every 15 min. The Yonsei University planetary boundary layer scheme (YSU PBL; Hong et al. 2006) and WRF single-moment microphysics class 5 (WSM5; Lim and Hong 2005) microphysics option were enabled. Results from additional experiments using the Mellor–Yamada–Janjić PBL scheme (Janjić 2002) revealed little sensitivity to the choice of PBL scheme (not shown). Convection was parameterized for the outermost domain only using the modified Tiedtke scheme (C. Zhang et al. 2011). WRF drag and enthalpy coefficients are calculated over the ocean as outlined in Dudhia et al. (2008), for which the drag coefficient saturates at high wind speeds.

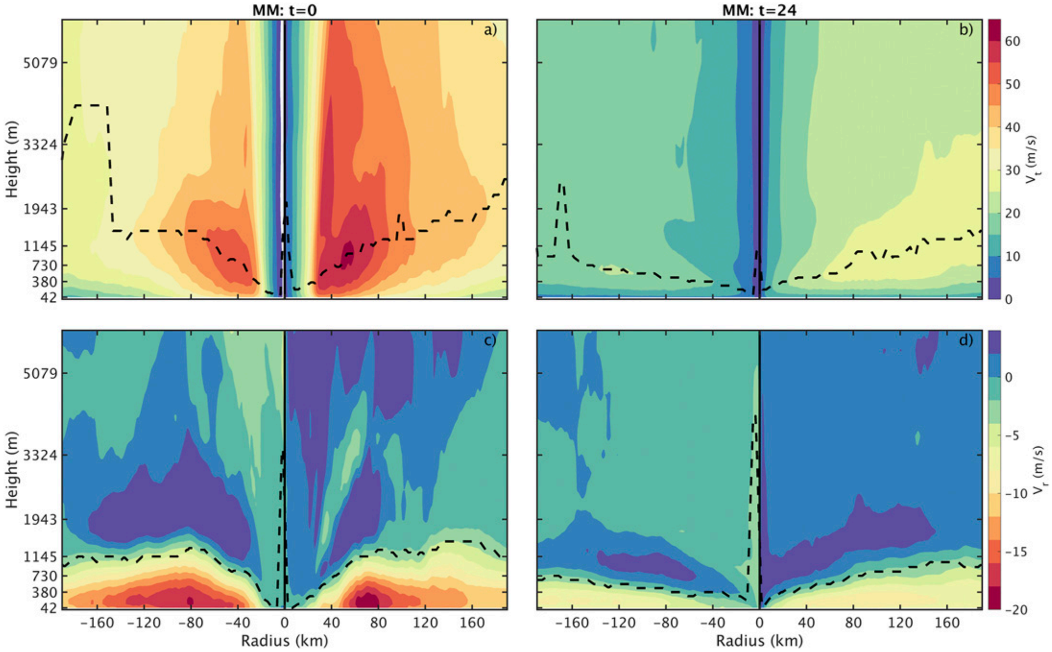

FIG. 4. Azimuthally averaged (a),(b) tangential winds and (c),(d) radial winds as a function of radius for the MM case at (a),(c) landfall and (b),(d) $t = 24$ h after landfall. Variables were averaged taken over the front (northwest and southwest; negative distance on the x axis) and rear (southeast and northeast; positive distance) storm-relative quadrants. Additionally, the TCBL height defined as (a),(b) the height of maximum tangential winds and (c),(d) the depth of the inflow (see text for definition) are plotted by the dashed black lines. The y-axis tick marks are placed every fourth unstaggered vertical level, starting with the lowest model level.

b. *Land surface sensitivity experiments*

The Noah land surface model (Noah LSM; Chen and Dudhia 2001) within WRF was used to calculate surface fluxes of heat and moisture over land. Landfall cases differed through prescribed surface roughness lengths Z_0 and volumetric soil water content S_c. The prognostic equation for soil temperature in the Noah LSM is a function of heat capacity C and thermal diffusivity K_t. Both variables are proportional to S_c multiplied by several parameters specific to each soil type. For consistency, we specified loam soil parameters for all simulations. Incoming solar and outgoing long-wave radiation schemes were disabled to remove the effects of the diurnal cycle, as this has been shown to impact surface fluxes significantly (Shen et al. 2002). We used four vertical soils levels extending down to 1.5 m.

Our control set of landfall cases consists of nine simulations. In this set, S_c and Z_0 were fixed in time and homogeneous across the land surface, while soil temperature varied in response to surface heat forcings. As shown in Table 1, the three S_c values tested are 0.05, 0.30, and 0.60, and for Z_0 are 5, 25, and 50 cm. These values will be referred to as dry, moderate, wet, smooth, moderate, and rough, respectively. The landmass initialized in each simulation was prescribed with one Z_0 and one S_c value. For example, the abbreviation RM indicates rough–moderate, i.e., $Z_0 = 50$ cm and $S_c = 0.30$. These values represent a wide yet realistic range of large-scale roughness and moisture conditions, based on a blend of values within the WRF USGS land-use table and various studies (Wierngal 1993). The dry value is akin to an arid region, while the wet value resembles a wetland environment such as the Florida Everglades. The smooth value represents a grassland environment, whereas the rough value simulates a large suburban zone or heavily forested region. C, K_t, and thermal inertia I_q—defined as the square root of the product of C and K_t—are shown in Table 2 for each S_c case, in addition to the values used for the two driest cases in T94 and the dry and wet sandy soil values representative of northern Australia, provided in E08, for reference. Our values of I_q for $S_c = 0.05$, 0.3, and 0.6 are similar to dry sandy soil, the soil case in T94, and wet soil, respectively. Also of note is that I_q of the second driest case in T94—shown in Table 2 as T94 dry—is actually much greater than any of the other cases shown, other than for an equivalent S_c value of 1.0, i.e., 100% soil saturation.

3. Structure before and during landfall

a. *TC evolution before landfall*

The intensity—evaluated using the maximum 10 m total wind speed $S10_{\max}$ (S indicates total wind speed), and minimum central pressure $P_{\min}$—from initialization of the ocean-only case is shown in Fig. 2. The ocean case reached category 1 hurricane designation by 24 h and rapidly intensified from $t =$ 36–60 h. Shortly after $t = 72$ h, each TC underwent an eyewall replacement cycle, evident by the sharp expansion of the radius of maximum winds (RMW) coinciding with weakening before and intensification afterward. Intensification resumed over the

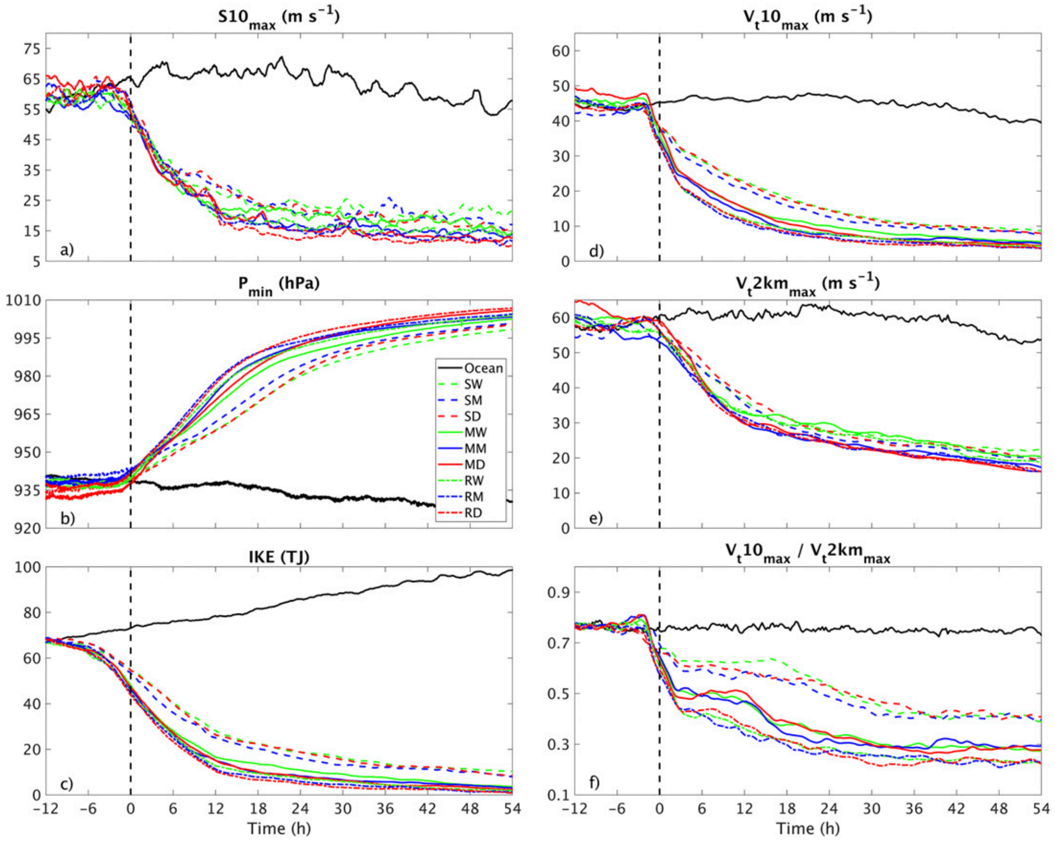

FIG. 5. (a) Maximum 10 m wind speed ($S10_{\max}$, m s^{-1}), with a 1 h running mean applied; (b) minimum surface pressure ($P_{\min}$, hPa); (c) integrated kinetic energy (IKE; TJ); maximum tangential wind speed at heights of (d) 10 m and (e) 2 km ($V_t10_{\max}$ and $V_t2\text{km}_{\max}$, respectively, m s^{-1}); (f) $V_t10_{\max}$ divided by $V_t2\text{km}_{\max}$. The ocean-only case is in black. Rough, moderate, and smooth Z_0 cases are in red, blue, and green, respectively. Wet, moderate, and dry S_c cases are in dashed, solid, and dot–dashed lines, respectively. Time on the x axis is shown relative to landfall, which is marked by the vertical dashed line.

next couple days, and each TC reached a lifetime maximum intensity (LMI) at roughly $t = 115$ h.

In all cases, a slow decline in $S10_{\max}$ and the maximum azimuthal-mean 10 m tangential winds ($V_t10_{\max}$, Fig. 2c) occurred a day before the landfall cases reach land. This contrasts the steady decrease in $P_{\min}$. We present three explanations for this behavior. First, idealized simulations of mature TCs commonly exhibit a slow decrease in maximum winds despite an increase in size. Kilroy et al. (2016a) attributed this behavior to the outward radial expansion of diabatic heating and dilution of vertical mass flux around the RMW. Figure 2c shows that the azimuthal-mean radius of tropical storm force winds continues to increase throughout the simulation time period despite intensity fluctuations, mirroring the findings of Kilroy et al. (2016a). Additionally, the azimuthal-mean tangential and radial winds shown in Figs. 3a and 3b expand outward from $t = 96$ to $t = 114$ h. Second, another eyewall replacement cycle finished between $t = 120$–132, which briefly limited further maximum wind intensification. Last, the low to moderate atmospheric vertical wind shear around the vortex had a slight influence on the vortex. Drying of the low-level azimuthal-mean equivalent potential temperature (θ_e) occurred below 2 km by $t = 114$ h, concomitant with increased coverage in negative vertical velocity beyond $r = 100$ km (Figs. 3c,d). This suggests that convective downdraft-induced drying of the low to midlevels may have contributed to dampening vortex intensification prelandfall. However, the simulated shear does not significantly affect our results. θ_e within 50 km increases in time, indicating that the inner core was unaffected by dry-air intrusions. Additionally, the 2–10 km vortex tilt with height never exceeded 6 km (not shown), as the vortices were powerful and deep enough to resist the shear.

Considering that these behaviors occurred within the ocean-only simulation, we can confirm that this slight decline in intensity observed for the landfall cases that began 24 h before landfall is not primarily due to land interactions. Additionally, each TC reached a steady-state before encountering land. We note that eyewall replacement cycle-like intensity fluctuations before landfall have been observed before in idealized simulations (Chen and Yau 2003; Williams 2019) and in observations (Wu et al. 2009). An in-depth investigation of prelandfall intensity changes due to the presence of land is beyond the scope of this study, and all further analysis will focus on the inland wind field and intensity decay. Additionally, from this point on, all time references are relative to the timing of landfall.

b. On the boundary layer height

As turbulence within the TCBL is primarily shear driven (Smith and Montgomery 2010; Zhang et al. 2011b; Kepert et al. 2016), we briefly present an analysis of the TCBL depth using two wind-based definitions: 1) the height of the maximum tangential winds and 2) the depth of the inflow, defined here as the depth at which the inflow reaches 10% of the maximum inflow as in Zhang et al. (2011a). Also plotted in Fig. 3 are the tangential (V_t, Figs. 3a,b) and radial (V_r, Figs. 3c,d) wind-based definitions (Figs. 3a,b) of the TCBL height over the ocean. The increasing height with radius as well as the depth of the TCBL are both consistent with observations and theory of the TCBL over the ocean (Eliassen 1971; Powell et al. 2003; Zhang et al. 2011a). The inflow-based definition is slightly deeper than the V_t-based depth within a radius of 100 km.

The V_t and V_r fields for the moderate Z_0, moderate S_c (MM) case are shown in Fig. 4 at landfall and $t = 24$ h after landfall. In this frame of reference, the TC moved from right to left. The TCBL heights defined above are also plotted over their respective fields. All variables were azimuthally averaged within the two front quadrants (negative values on the x axis) and the rear quadrants (positive values). At landfall, the deeper mixing resulting from interaction with the rough land surface deepens the TCBL as defined by both definitions compared to the ocean case, in agreement with previous findings (Knupp et al. 2006; Zhang and Pu 2017). After 24 h inland, the strength of the wind field and thus turbulent mixing significantly decreased, and the TCBL height decreased to below 1 km within a radius of 200 km by both metrics. Additionally, by this time the RMW had expanded beyond the limits of the innermost domain.

4. Intensity and wind field decay

a. Intensity decay

Figure 5 shows time series of $S10_{\max}$, $P_{\min}$, integrated kinetic energy (IKE) (defined below), $V_t10_{\max}$, and the maximum azimuthal-mean tangential winds at 2 km height ($V_t2\mathrm{km}_{\max}$) for the control set. Rapid weakening in $S10_{\max}$ and $P_{\min}$ began roughly 2 h before landfall for all cases. By 12 h inland, the majority of the weakening had already occurred, as each TC had degraded from minimal category 4 at landfall to tropical storm or weak category 1 status by this time. Weakening continued throughout the simulation time period, albeit at an increasingly slower rate. After being inland for 12 h, intensities for the smooth Z_0 cases were greater than that of the rough cases by approximately 15 m s^{-1} and 20 hPa, indicating a slower initial intensity decay for decreasing Z_0. Differences in $S10_{\max}$ and $P_{\min}$ between S_c cases did not vary much initially. However, during the slower weakening period beyond 12–24 h, the wet simulations were stronger than the moderate and dry cases by a few meters per second and hectopascals. Note that differences on the order of a few meters per second and hectopascals by this time reflect a larger percentage of the overall intensity.

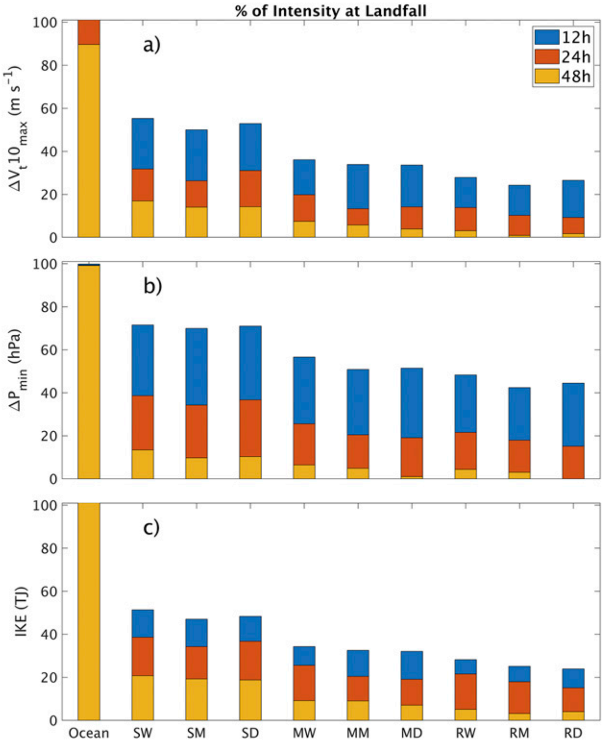

FIG. 6. Percentage of the landfall intensity represented by the (a) $\Delta V_t10_{\max}$, (b) $\Delta P_{\min}$, and (c) IKE metrics for the control set. Blue, red, and green bars respectively indicate 12, 24, and 48 h after landfall or time of lifetime maximum intensity. The ocean-only percentage of intensity is relative to the intensity at 132 h after ocean initialization, within an hour of when the landfall cases made landfall. Note that the ocean case changes in intensity are negligible within 24 h.

To evaluate the destructive potential of the entire wind field, IKE is plotted in Fig. 5c. Similar to Powell and Reinhold (2007), we define IKE as (1), i.e., the volume-integrated kinetic energy at 10 m:

$$\mathrm{IKE} = \frac{1}{2}\int \rho (S10)^2\, dV. \tag{1}$$

For simplicity, we integrated over a 1 m cube centered at 10 m over the entire innermost domain. The value of ρ was a constant 1 kg m^{-3}. Prelandfall decay began 12 h before landfall, several hours earlier than for $S10_{\max}$ and $P_{\min}$. This was due to IKE accounting for the immediate reduction of the outer wind field over land ahead of the TC. Additionally, the fastest rate of IKE decay occurred at landfall, as roughly half of the cyclonic wind field was directly over land at this point. This differed from $S10_{\max}$ for which the decay rate was greatest 2–3 h inland. As with the previously mentioned two metrics, the decay rate slowed after 12 h inland. The smooth Z_0 cases maintained a larger intensity than the moderate and rough cases throughout the simulation period by approximately 10 TJ. Differences between S_c cases were negligible during the rapid weakening period and minimal during the slow weakening period; however, the wet cases maintained a slightly larger inland intensity by a few TJ for the moderate and rough Z_0 cases.

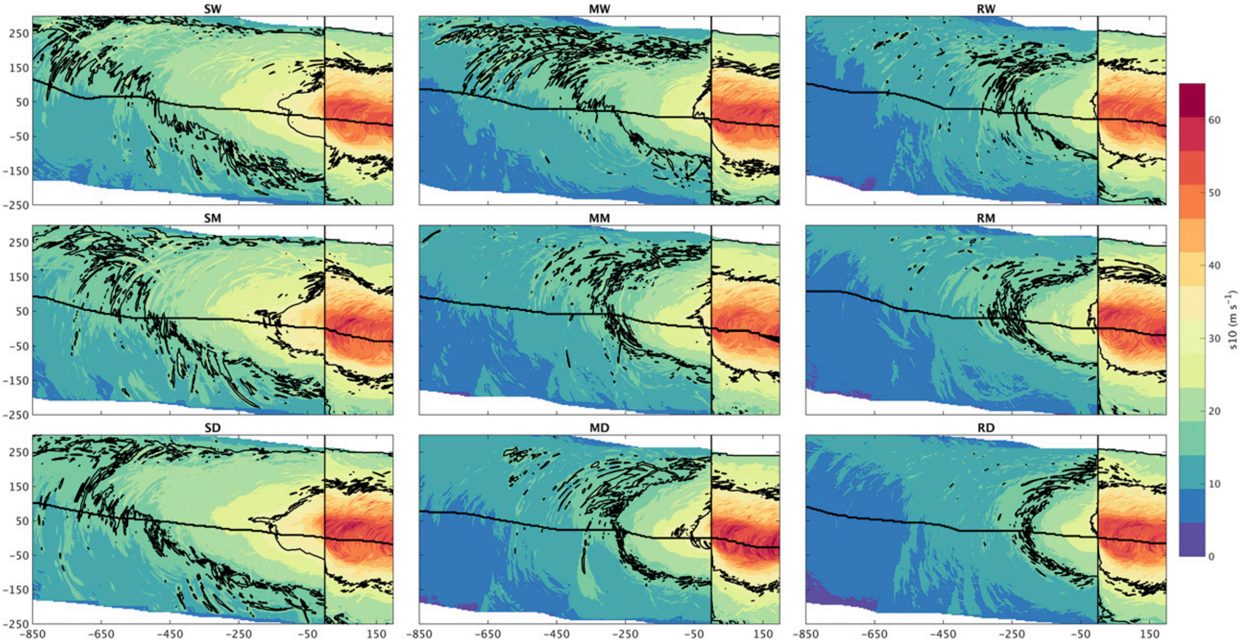

FIG. 7. $S10$ surface wind footprint, i.e., the maximum 10 m wind speed at every point near landfall across the duration of each simulation. Vertical black line shows the location of the coast. Axis units are distance from the location of landfall (km). Black contours show the tropical storm and category 1 force wind area. TC track is shown by the black line running perpendicular to the coast. TCs are moving from left to right in this frame of reference.

Figure 6 shows intensity as a percentage of the intensity at landfall at three times: 12, 24, and 48 h after landfall. Because of the inherent volatility in $S10_{\max}$, $V_t10_{\max}$ is used instead. Pressure and $V_t10_{\max}$ percentages were calculated by converting $P_{\min}$ to $\Delta P_{\min}$ and $V_t10_{\max}$ to $\Delta V_t10_{\max}$, or the difference in TC intensity at each time from the intensity of the ocean-only case at the simulation start, e.g., $\Delta P_{\min}(t) = 1005\,\text{hPa} - P_{\min}(t)$ and $\Delta V_t10_{\max}(t) = V_t10_{\max} - 3.6\,\text{m s}^{-1}$. The $\Delta V_t10_{\max}$ and IKE decay by 40%–60% within 12 h. The $\Delta P_{\min}$ decayed at a slower rate than the other two metrics, suggesting that the vortex warm-core structure was maintained inland for a longer duration. The smooth cases were stronger within $t = 12$–24 h than the moderate and dry Z_0 cases by approximately 10%, while differences between S_c were smaller. Note also that the constant Z_0 moderate S_c simulations are weaker across most metrics within 12 h, a trend also observed in Figs. 5a–d. We will discuss this result in section 5b.

We return to Figs. 5d–f to compare the strengths of the circulations at 10 m and above the TCBL at 2 km (Fig. 4). The decay of $V_t10_{\max}$ was similar to that of $S10_{\max}$. However, the rate of decay of $V_t2\text{km}_{\max}$ was slower within the initial 12 h inland, after which the circulation above the TCBL steadily decreased at an almost linear rate. Additionally, differences in $V_t2\text{km}_{\max}$ between cases was smaller, except that the smooth Z_0 cases were stronger than moderate and rough Z_0 throughout by roughly 10 m s^{-1}. During the slow decay phase beyond 24 h, the difference between the wet S_c cases and the moderate and dry S_c cases grew. Figure 5f shows the ratio of $V_t10_{\max}$ to $V_t2\text{km}_{\max}$. This ratio was highly sensitive to Z_0, decreasing from around 0.75 for the ocean-only case to 0.6, 0.5, and 0.4 after 12 h for the smooth, moderate, and rough Z_0 means. The sensitivity to S_c was negligible, even as the decay slowed.

To summarize this section, Z_0 and S_c affected intensity decay at different stages in the decay process. The first 12 h within landfall was characterized by a rapid decay of the near-surface circulation for all surface cases. The decay was more sensitive to changes in Z_0 than for S_c. Once the TC moved inland and substantial weakening occurred, S_c played an increasingly greater role in influencing the 10 m intensity and the strength of the 2 km circulation. Additionally, the surface circulation decayed faster than the circulation above the TCBL.

b. *Quantifying the broader wind field decay*

Figure 7 shows the 10 m maximum wind speed footprint for the control set. As with intensity, differences near the coast were driven mostly by Z_0; along-track hurricane force winds for the smooth Z_0 cases occurred out to 150 km from the coast compared with 50 km for the rough cases. Similarly, tropical storm force winds extended much farther inland and to the right of track for the smooth cases, approximately 850 km inland compared to 250 km for the rough cases. Differences between S_c cases are less apparent than for Z_0; however, tropical storm force winds for the wet cases extended farther inland and to the right of the track than for the moderate and dry cases.

Figure 8 shows the azimuthally averaged RMW and radius of tropical storm force winds (TSR) at 10 m, averaged among the smooth, moderate, and rough Z_0 cases (Fig. 8a) and wet, moderate, and dry S_c cases (Fig. 8b). All TCs experienced a broadening of the RMW and a contraction of the TSR with increasing time inland. Both of these processes are reflected in

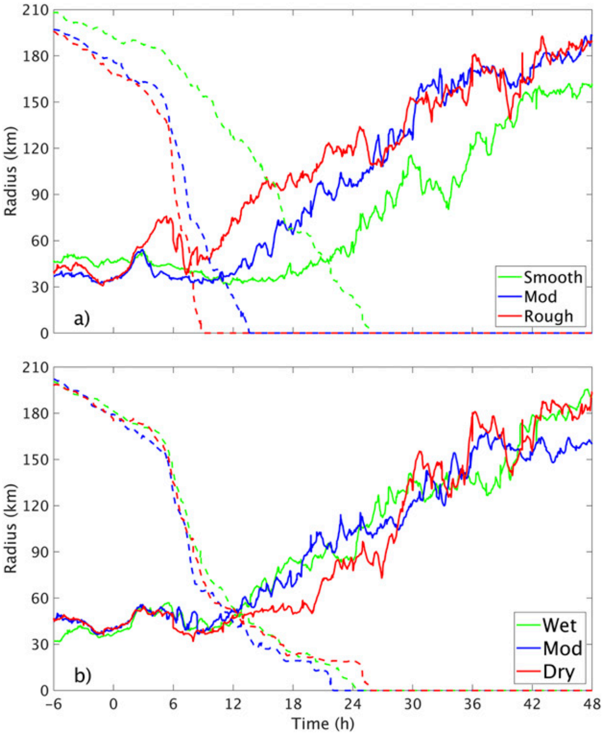

FIG. 8. Azimuthal-mean RMW (solid lines) and radius of tropical storm force winds (dashed lines) at 10 m. (a) Ensemble mean smooth (SW, SM, SD; green), moderate (MW, MM, MD; blue), and rough (RW, RM, RD; red) simulations. (b) Ensemble-mean wet (SW, MW, RW; green), moderate (SM, MM, RM; blue), and dry (SD, MD, RD; red) simulations. The x axis marks the time since landfall.

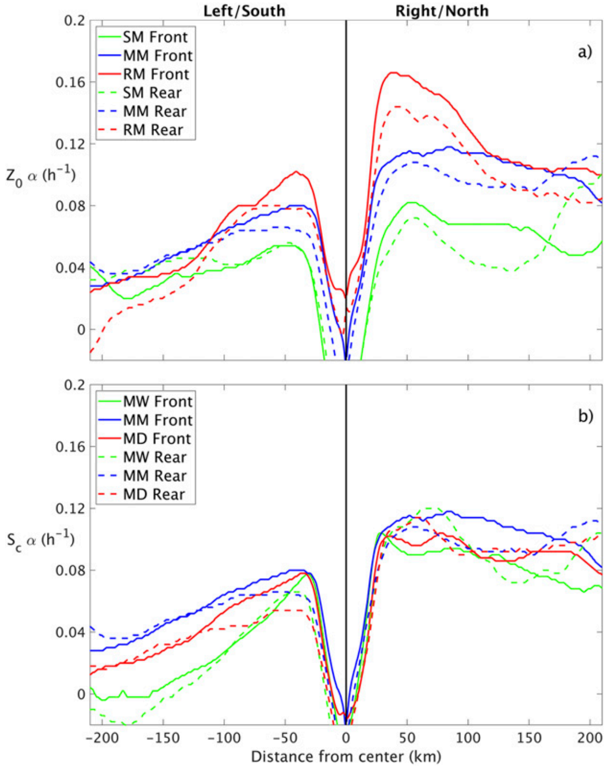

FIG. 9. $\alpha(r)$ (h^{-1}) for (a) smooth (green), moderate (blue), and rough (red) Z_0 moderate S_c and (b) moderate Z_0, wet (green), moderate (blue), and dry S_c by TC quadrant. Positive (negative) radii show the right (left)-of-motion quadrant-averaged $S10$, and solid (dashed) lines indicate the front (rear) quadrants. The TC is moving into the page in this frame of reference.

Fig. 7; while the entire wind field was contracting, the location of the maximum surface winds shifted farther to the right of the track. The rate of RMW expansion was more sensitive to Z_0 than to S_c, as increasing roughness amplified both the RMW expansion rate and TSR contraction. Meanwhile, the RMW expansion rate for the wet and moderate S_c cases was slightly greater from $t = 12$–20 h of landfall than for the dry cases. After this time, the dry cases experienced a more rapid expansion. At the same time, the TSR is modestly larger for the wet cases than for the moderate and dry cases by approximately 10 km. The change in relative wet and dry RMW expansion rates are expounded in section 5b.

To quantify the decay rate of the wind field as a function of radius, we turn to the empirically derived decay model of KD95:

$$V(t) = V_b + (RV_0 - V_b)e^{-\alpha t} - C, \tag{2}$$

where $V(t)$ is the predicted inland maximum wind speed, V_b is a constant background value to which the winds asymptotically approach, V_0 is the wind speed at landfall, R is a roughness scaling factor, and α is the e-folding time decay constant. Larger α indicates a faster rate of decay. C is a quadratic function of distance and time inland that KD95 calculated using best-fit analysis. $t = 0$ indicates the time of landfall. Inclusion of the KD95 decay model and subsequent iterations within the Statistical Hurricane Intensity Prediction Scheme (SHIPS) has vastly improved the model's TC inland intensity forecasts, especially within 0–72 h (DeMaria et al. 2005). The difference between (2) and our version used in this study, shown below as (3), is that we computed $S10_{\text{decay}}$ as a function of radius:

$$S10_{\text{decay}}(r,t) = S10_b + [R(r)S10_0(r) - S10_b]e^{-\alpha(r)t}. \tag{3}$$

Additionally, we neglect term C in (2) as this vastly increased errors, likely because KD95 found that a portion of inland TCs strengthen through baroclinic processes related to the strong midlatitude horizontal temperature gradient which was absent in our simulations. All variables correspond to those of KD95 for our $S10$ fields. We solved (3) for the optimal α and R that best correlated with the actual radial decay of each simulation. To do this, we first transformed the wind field to a storm-centric cylindrical coordinate system, and then azimuthally averaged within four quadrants: the northeastern, northwestern, southwestern, and southeastern quadrants. Since each TC translates approximately due westward, we refer to these quadrants in motion-relative terms: right rear, right front, left front, and left rear, respectively. Equation (3) provided us with reasonable estimates of decay rate, as applying (2) and (3) to the intensity decay time series for each TC (Fig. 5a) produced

r^2 values between 0.95 and 0.98 for each simulation. Additionally, our values for α obtained using (3) for the peak winds near the RMW in Fig. 9 closely match those of KD95, as they found α of 0.095 and 0.080 h^{-1} for $R = 0.9$ and 0.8 at the RMW, respectively. Our range of R values consistently landed between 0.95 and 1.05, only slightly higher than 0.8–1.0, which KD95 found to best fit observations.

Figure 9 shows α for each quadrant of SM, MM, and RM, and MW, MM, and MD. We do not show similar plots for the other TCs in our control set, as the following relationships are nearly identical across all cases. The pattern of $S10_{\mathrm{decay}}$ was highly asymmetric and varied by radius. Figure 9 provides two indications that initially stronger winds at landfall decayed faster. First, α increased toward the RMW. Second, α is larger to the right of motion and generally in the front quadrants, where the inland winds were stronger. In addition to the acceleration provided by the motion asymmetry, the residence time of air parcels to the left of motion over land was longer within the first few hours after landfall, which slowed the circulation further. The fact that initially stronger winds decayed faster makes sense intuitively, as the greater difference in momentum between the strongest winds and the surface forces a greater response. It is important to note that the outwards expansion of the RMW during weakening (Fig. 8) likely slowed decay rates outside of a radius of 40 km below what they may have been for a static RMW. Additionally, the decay rate reached a local maximum near the edge of the domain due to the contraction of the overall size of the TC during weakening (Fig. 8), as the far outer-core winds at large radii reached $S10_b(r)$ more quickly. There is a clear sensitivity to Z_0 as well, as α increases with Z_0 across the domain within the right two quadrants and within roughly 100 km within the left two quadrants.

Conversely, the decay rate within 100 km was less sensitive to differences in S_c (Fig. 9b) than for Z_0. The sensitivity to S_c mainly existed in the broader wind field and to the left. Beyond the RMW, α was actually largest for MM and smallest for MW. This suggests that a soil moisture value of 0.3 may provide the least favorable environment for a TC, further supported by the lower inland intensity of the moderate S_c cases from section 4a and from Figs. 5 and 6.

c. Changes to the S10 radial profile during landfall

Figure 9 also shows that α was slightly negative within the initial RMW for all cases, indicating that winds at small radii *increase* in time. Figure 10 shows the azimuthal-mean radial wind speed profile at 10 m at 5 different times from $t = 12$ h before landfall to $t = 24$ h after for SM, MM, and RM. Before landfall, the radial profile reflected a U-shaped increase with increasing radius within the RMW and a steady weakening with increasing radius beyond the RMW. At landfall, the radial profile reflected a more typical Rankine vortex with winds increasing linearly from $r = 0$. After landfall, the strong winds at the RMW weakened while the radial shape inside the RMW became more convex as winds increased. By 24 h inland, the radial profile in each case was fairly flat, and the RMW had expanded greatly. This process occurred sooner for increasing Z_0, indicating a more rapid change in the profile shape for increasing roughness. We note that total wind speeds at $r = 0$ are greater than zero due to the TC movement.

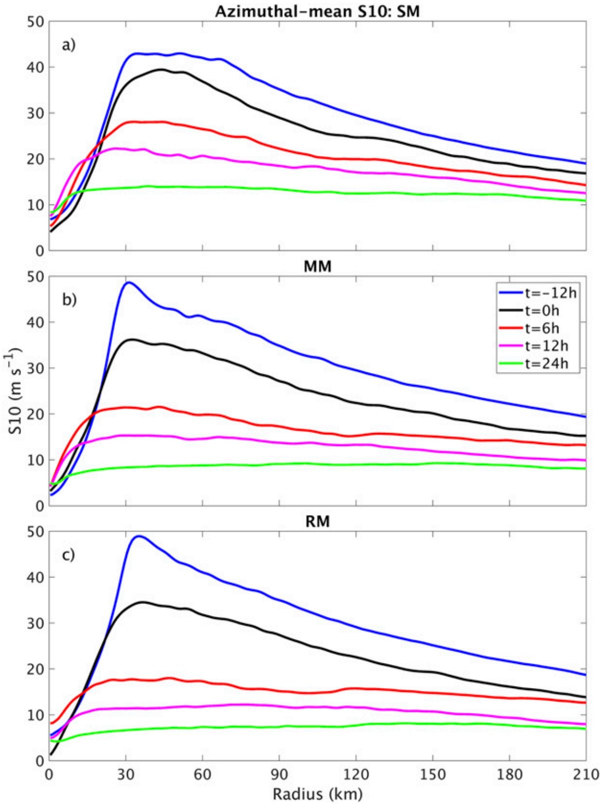

FIG. 10. Azimuthally averaged $S10$ as a function of radius at five times: 12 h before landfall (blue), at landfall (black), and 6 (red), 12 (magenta), and 24 (green) h after landfall for (a) SM, (b) MM, and (c) RM.

The relationship between the rapidity of the broadening of the radial wind profile and Z_0 follows from the changes in the TCBL structure during landfall. Figure 11 shows the inward advection of angular momentum by the radial inflow M_{adv}, as well as contours of radial velocity (black) and total wind speed (white). All three fields are azimuthally averaged within the forward quadrants—i.e., western quadrants—3 h before, during, and 3 h after landfall. Before landfall, the greatest M_{adv} is located below a height of 300 m for both the SM and RM cases. The inflow in RM is slightly deeper and stronger due to the greater convergence of the onshore flow caused by the rougher surface upstream and enhanced offshore inflow (not shown). Consequently, M_{adv} within the TCBL is greater for RM than for SM. This led to a larger radial gradient of the total winds for RM near the RMW. An outflow layer was also present directly above the inflow layer (Fig. 11, dashed black contours). At landfall, the radial inflow observed for RM was much deeper vertically and penetrated farther inward toward the TC center than in SM, which enhanced M_{adv} below 1 km and within a radial band 20–50 km from the center. Consequently, the total wind speed and the radial gradient of the total wind speed below 500 m were both stronger within a radius of 30 km, despite the greater reduction in near-surface winds at larger radii. This stronger inflow in RM was compensated for by a stronger outflow layer between heights of approximately 1–3 km, which

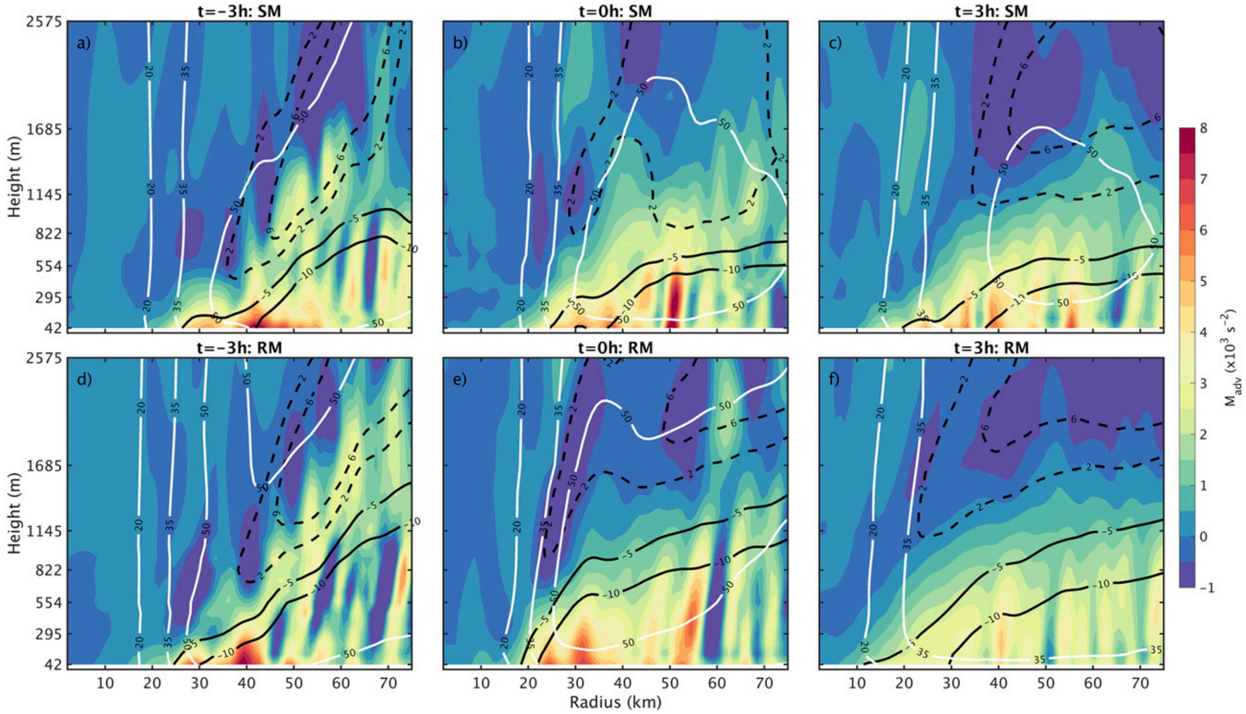

FIG. 11. Azimuthally averaged advection of angular momentum M by the inflow and vertical winds (M_{adv}, colored contours, in $10^3\,s^{-2}$, where positive values indicate advection toward the center and/or away from the surface), radial velocity (V_r, inflow in solid black contours of -10 and $-5\,m\,s^{-1}$ and outflow in dashed black contours of 2 and $6\,m\,s^{-1}$), and total wind speed (S, solid white contours of 20, 35, and $50\,m\,s^{-1}$) for (a)–(c) SM and (d)–(f) RM as a function of radius at three times: (a),(d) 3 h before landfall, (b),(e) at landfall, and (c),(f) 3 h after landfall. M_{adv}, V_r, and S are azimuthally averaged within the front (i.e., western) two quadrants.

transported M away from the center. After 3 h inland, the inflow layer remained deeper for RM than for SM and winds above 100–200 m were more intense for RM, which can be seen by comparing the 20 and $35\,m\,s^{-1}$ contours in Figs. 11c and 11f. However, total near-surface winds across much of the TC had already decayed more than for SM. The near-surface M_{adv} for RM outside of a radius of 20 km decreased, yet increased within a radius of 20 km.

In summary, the discontinuity in Z_0 at the coastline forced an acceleration of the secondary circulation below 3 km. This led to a brief enhancement of the near-surface total wind field at and within the initial RMW within 3 h of landfall, which was amplified for larger Z_0. After a couple hours, however, the near-surface winds for RM decayed quickly and the radial profile of 10 m wind speed flattened out more rapidly than for SM, increasing wind speeds inside of the initial RMW. This mechanism may explain why the $S10_{max}$ decay rates for all Z_0 cases in Fig. 5a are similar within 6 h, as the rough surface temporarily boosts the maximum winds. The other intensity metrics reflect weaker TCs for increasing Z_0, indicating that the $S10_{max}$ metric is not a good reflection of the overall strength of the TC.

5. Analysis of the low-level thermodynamics

We now examine the thermodynamics of the lower TCBL to understand the initial lack of sensitivity to S_c and why this sensitivity increased in time. For brevity, we focus on the moderate Z_0 cases with wet, moderate, and dry S_c; however, the results apply across the smooth and rough Z_0 cases as well, except where otherwise stated.

a. *The relationship between S_c and surface heat fluxes*

Figures 12a–f compares instantaneous surface temperatures for MW, MM, and MD within the innermost domain at 3 and 30 h after landfall, representing differences during the rapid and slow decay phases. After 3 h inland, all cases featured land surface temperature depressions of several degrees Celsius within tens of kilometers radius, as the strong cyclonic winds rapidly extracted heat from within the low thermal inertia soil. This is in contrast with heat exchanges over the ocean, where the deep ocean mixed layer and high thermal inertia of water result in smaller changes in temperature. Also unlike over the ocean, the greatest inland cooling occurred underneath the TC center, leading to a more symmetric surface cold patch. Over most of the outer domain, the MW case featured the coolest surface temperatures, due to increased evaporational cooling of the soil moisture. MM featured the lowest inner core temperatures, and temperatures cooled the least for MD. At $t = 30$ h, cooling was widespread and greatest for MW and MD.

Figures 12g–l compares model-derived radar reflectivities at the lowest model level at $t = 3$ and 30 h. The surface cooling correlates exceedingly well with reflectivity—which is essentially a proxy for precipitation—due to the localized intensification of surface wind speeds. Precipitation occurred over a

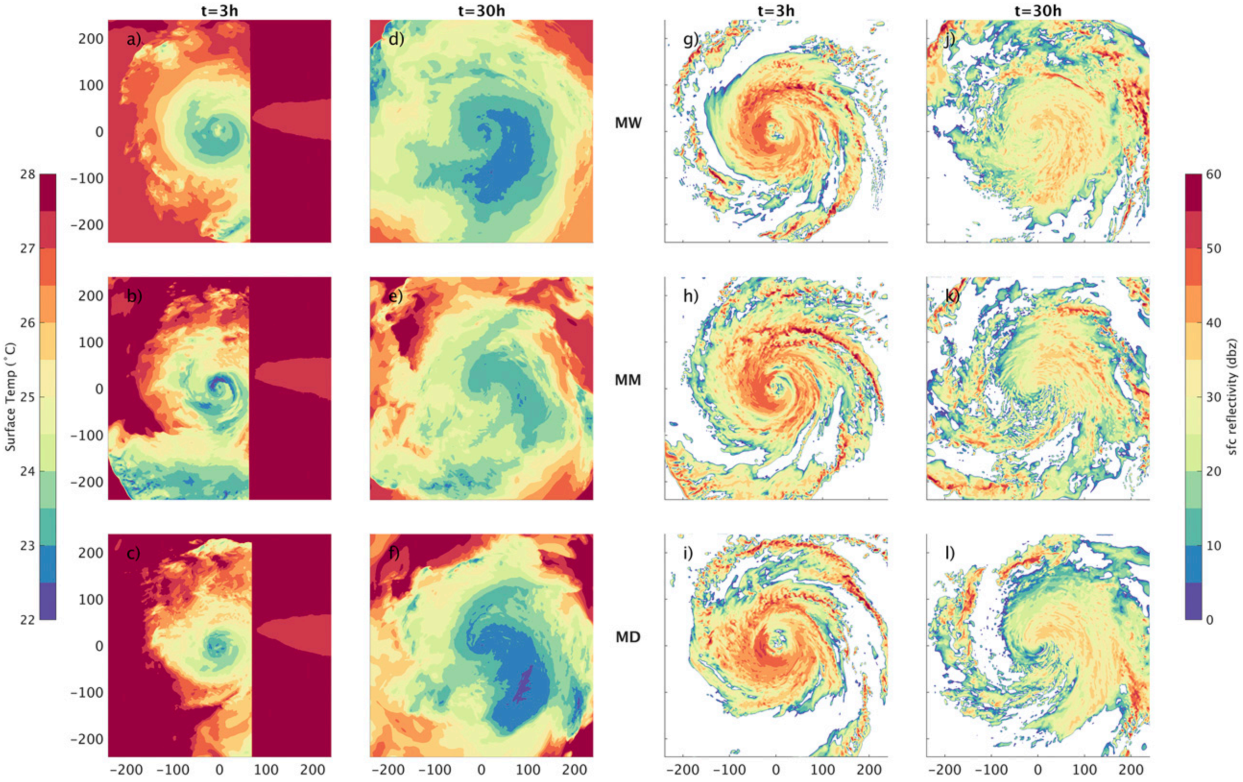

FIG. 12. Contoured (a)–(f) surface temperature (in °C) and (g)–(l) model-derived radar reflectivity field at the lowest resolved model level (in dBZ) over the innermost nested domain for (top) moderate Z_0 wet, (middle) moderate, and (bottom) dry S_c at two times: (a)–(c),(g)–(i) 3 and (d)–(f),(j)–(l) 30 h after landfall. The axis show distance (in km) from the TC center. In all panels, the TCs are moving from east (left) to west (right). Note that a portion of the eastern TC circulation is over water at t = 3 in (h).

broader area within t = 3 h for MM than for MD and MW, despite the greater available surface moisture supply for MW. Consequently, inner-core surface temperatures were lowest for MM by t = 3, as enhanced localized winds stimulated by convection further cooled the surface. Conversely, by t = 30 h when all TCs were much weaker, domainwide precipitation broadened for increasing S_c.

Despite the greater moisture supply for MW and the other corresponding wet S_c cases, the MW convective activity within a few hours of landfall was comparable to that of the dry cases. The enhanced cooling for increasing S_c appears to be the culprit for the limited development of MW. Figure 13 shows time series of domain-mean surface latent and sensible heat fluxes LH and SH as well as surface temperature across the innermost domain for each simulation in the control set. Over the ocean, LH dominated SH by as much as an order of magnitude. LH decreased rapidly in all cases to the point where LH and SH were of comparable magnitude by t = 12 h inland. The key aspect of this figure is that inland domain-averaged LH was greater and SH was more negative for increasing S_c, as the greater evaporation of soil moisture cooled the surface. Additionally, cooler surface temperatures lower the saturation vapor pressure of the near-surface air, limiting the potential for further sustained LH. Thus, increasing S_c led to only a slight overall increase in net heat fluxes, on the order of a few watts per square meter across the innermost domain of the wet cases.

To summarize, the cooling of the surface via soil moisture evaporation countered the increased moisture availability, limiting development of the wet cases within several hours of landfall. Referring back to Figs. 5 and 6, the moderate S_c cases remained slightly weaker than the wet and dry cases throughout. Additionally, Fig. 9b revealed greater decay rates for MM. However, the MM environment was initially the most supportive for convection. It appears that the combination of initially warm surface temperatures for MM within a few hours of landfall and the sufficient inland moisture supply was enough to overcome the negative effect of surface cooling. So why were the moderate moisture intensities weaker than the wet or dry cases over the course of almost the entire simulation period? Figure 13 reveals that the moderate S_c was only optimal for a few hours. Averaged surface temperatures dropped quickly for MM by 6 h for each moderate S_c case, coincident with a drop in both LH and SH. Likely, the TCs that encountered the moderate environment extracted heat from the surface more quickly than for the dry or wet environments, leading to a brief but unsustainable burst of convection. As inland conditions deteriorated, the moderate S_c TCs failed to rejuvenate and overcome the initial rapid weakening.

b. On the timing of the heightened sensitivity to S_c

In the previous subsection, we discuss how the enhanced cooling observed for the wet S_c simulations stifled further

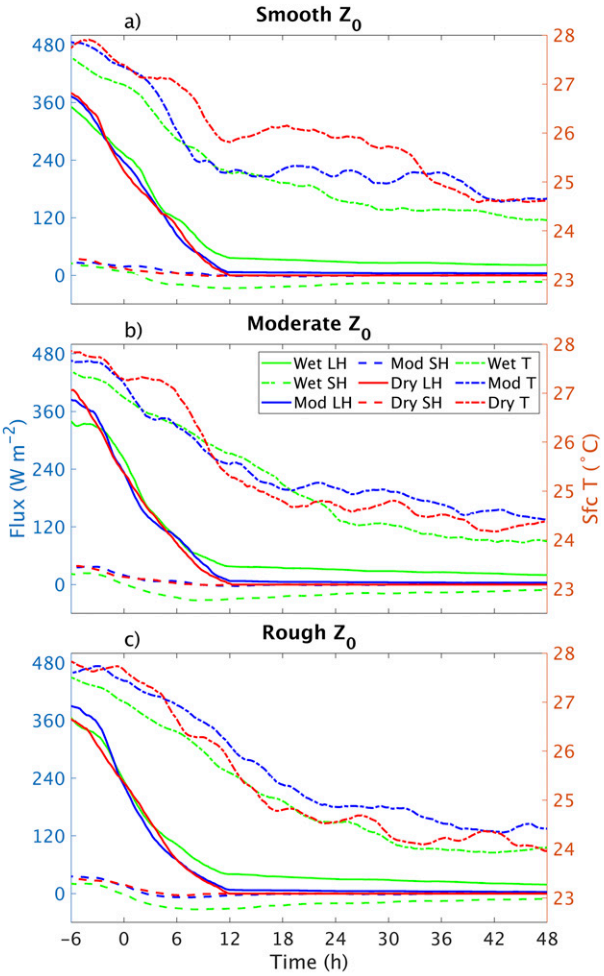

FIG. 13. Time series of the mean latent (solid) and sensible (dashed) fluxes (W m^{-2}, left axis) and mean surface temperature (dashed–dotted, right axis) averaged within the innermost domain for (a) smooth, (b) moderate, and (c) rough Z_0. Wet, moderate, and dry simulations are shown in green, blue, and red, respectively. Positive (negative) values indicate upward (downward) fluxes. Surface temperature averaged within the same circle is plotted in time, shown by the dashed–dotted plots.

intensification within 12 h. The question remains as to why the sensitivity of the near-surface wind decay to S_c increased starting around $t = 12$ h. Figure 13 shows that SH for the MW case reached a minimum between $t = 6$–12 h, and trended toward zero in time as the surface wind stress weakened. LH weakened in time as well but remained larger in magnitude than SH, leading to an increasingly net positive in overall enthalpy fluxes after $t = 12$ h on the order of a few watts per square meter. Thus, an obvious explanation is that weaker TCs can persist on lower surface enthalpy fluxes (E08; Montgomery et al. 2009; Evans et al. 2011; Tang et al. 2016). In addition, we present a supporting hypothesis: TCs in moist environments benefit from high S_c once the RMW expands to a sufficient radius.

Figure 14 shows Hovmöller diagrams of the azimuthally averaged diabatic heating rate Q—vertically averaged between 2 and 6 km—for MW, MM, and MD. As over the ocean, Q is greatest near the RMW within roughly 6 h inland. Greater outer-core Q occurred for MM within 3 h inland, in accordance with increased convection. After 3 h, Q beyond a radius of 80 km increased quickly for MW and decreased for MM and MD. Thus, LH in MW was sufficient to sustain more moist convection beyond 6–12 h than for MM or MD.

By $t = 9$ h for each case, the RMW within 2–6 km height began to expand rapidly outwards as the strongest winds decayed quickly, coinciding with a broadening in Q. By $t = 12$ h, large concentrations of Q for MW became located within the RMW, and the outward expansion of the lower-tropospheric RMW slowed. This decrease in the outward expansion occurred in all cases. However, expansion continued to slow significantly for MW while the lower-tropospheric RMW for MM and MD continued to expand. In fact, the 2–6 km RMW resided beyond the innermost domain by $t = 18$–19 h for MM and MD while the RMW at these heights for MW remained within the domain until $t = 27$ h. The 10 m RMW—shown by the white dashed plots in Fig. 14—followed a similar yet delayed progression. Expansion occurred later for drier environments; however, the rate of expansion after $t = 18$ h increased for drier environments, which can also be seen in Fig. 8.

Midlevel heating is most efficient at accelerating V_t at the RMW when the bulk of Q occurs within the RMW, as the inertial stability is usually greater within this region (Schubert and Hack 1982; Vigh and Schubert 2009; Kilroy et al. 2016a). As each cyclone decayed and domainwide convection became diluted, Q aligned within the expanded RMW beyond $t = 11$ h. Relating this to the sensitivity of the TC intensity to S_c (Fig. 5), the wet case intensities began to decay at increasingly slower rates by $t = 12$ h. Higher Q outside of the RMW within the wet cases did not favor further intensification of $S10_{\max}$ and $P_{\min}$ over the dry cases within $t = 6$ h, and not until $t = 12$ h in terms of IKE and $V_t10_{\max}$. These trends are more apparent for increasing Z_0.

Ultimately, the loss of momentum to the rough surface and the low surface enthalpy fluxes resulted in the continual demise of each TC. However, these results suggest that increasing S_c aided in slowing weakening beginning at the time at which significant relocation of concentrated Q within the lower-troposphere RMW occurred. Additionally, enhanced outer-core convection in the wet cases locally increased outer-core surface winds regardless of the position of the RMW, as observed in the wind footprints of Fig. 7 and the TSR shown in Fig. 8b. This led to a larger TSR for the wet cases and a slower decay rate.

Last, it is possible that the limited outer-core convection for the dry cases contributed to a focusing of Q at smaller radii seen in Fig. 14. This would seem to preserve the intensity of the TC at the expense of the overall size of the circulation. The higher intensities of the dry cases relative to the moderate cases in Figs. 5 and 6 and the smaller wind field for the dry cases in Fig. 7 insinuate this. Additionally, Fig. 5e reveals that the intensity of the 2 km circulation of the dry cases exceeded that of the wet and moderate case circulations for each Z_0 within $t = 6$–12 h. In contrast, Fig. 8b reveals that the mean TSR for $S_c = 0.05$ extended beyond that of the other two values around

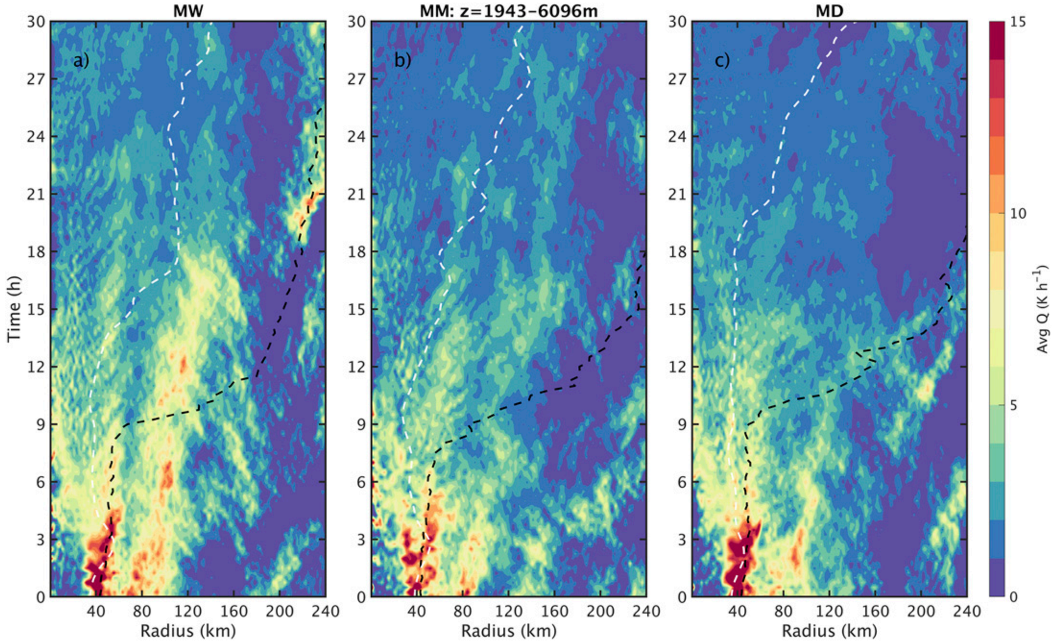

FIG. 14. Azimuthally averaged diabatic heating rate Q (colored contours, in K h^{-1}), vertically averaged within the model levels closest to 2 and 6 km, as a function of time and radius for (a) MW, (b) MM, and (c) MD. The average RMW between the same vertical levels as for Q (dashed black line) and the 10 m RMW (dashed white line) are also plotted. The time axis marks the hour since landfall.

t = 21–25 h. However, after removing the smooth cases from that composite, the TSR is lowest for dry (not shown). Therefore, it appears that SD may have been an outlier case, or alternatively, the smooth Z_0 enabled wind expansion to a greater degree than the dry surface disabled it.

c. *Sensitivity to soil physics*

To further emphasize the correlation between surface heat fluxes and S_c, we performed three additional sets of MW, MM, and MD simulations. Two of these sets—T26 and T28—were performed with constant land surface temperatures of 26 and 28°C. The third set—VSC—permitted S_c to vary in time and space due to precipitation and evaporation, in addition to varying land surface temperatures.

Figure 15 shows the mean heat fluxes—and for VSC the mean surface temperature—within the innermost domain for the three sensitivity sets. Inland LH was similar between T26 and T28; the wet cases featured elevated LH, which was low for the moderate and dry cases. SH and LH were roughly equivalent for each S_c case within T26, while SH was approximately twice as large as LH for T28. In VSC, rainfall saturated the soils within roughly 120 km for all three simulations (not shown), enhancing LH. The wet VSC cases still featured the greatest domain-mean LH, owing to the greater moisture supply outside of regions of heavy precipitation. Consequently, SH was increasingly negative for increasing S_c. Overall, the magnitudes of SH and LH were greater than for the control set, resulting in similar net enthalpy fluxes between VSC and the control set.

Figure 16 shows time series for $S10_{\max}$, $P_{\min}$, and IKE for the sensitivity sets, similar to Fig. 13. The spread in intensities between cases was much closer than for the control set. T28 is only marginally more intense throughout than T26, and both are slightly more intense than the control set and VSC by a few meters per second, TJ, and 10 hPa. Differences are mainly apparent after 12 h inland. The differences in LH are a smaller percentage of the total enthalpy fluxes for T26 and T28 due to the higher SH; thus, the sensitivities to S_c are even less apparent in these simulations than for the control set. The wet cases in these two sets were marginally more intense throughout than the moderate and dry counterparts, however. In VSC, the disparity between the S_c cases was larger than in T26 and T28, as decreased SH plays an important role in limiting enthalpy fluxes. VSC was similar to the control set in that the wet case was more intense inland than dry and moderate S_c. One difference between the VSC and control set is that the moderate S_c case was not weaker than the wet or dry cases in VSC. This indicates that the unfavorable moderate regime may not exist when soil moisture contents vary, likely due to the larger LH overcoming the surface cooling, as for the wet cases of the control set.

6. Summary and discussion

In this study, idealized TCs were subjected to a range of different inland soil moisture and surface roughness lengths to test the sensitivity of the inland near-surface wind field decay to realistic surface conditions. Our main results are summarized below.

1) Immediately after landfall, the 10 m winds rapidly decayed. Intensity decay was more sensitive to Z_0 than to S_c within

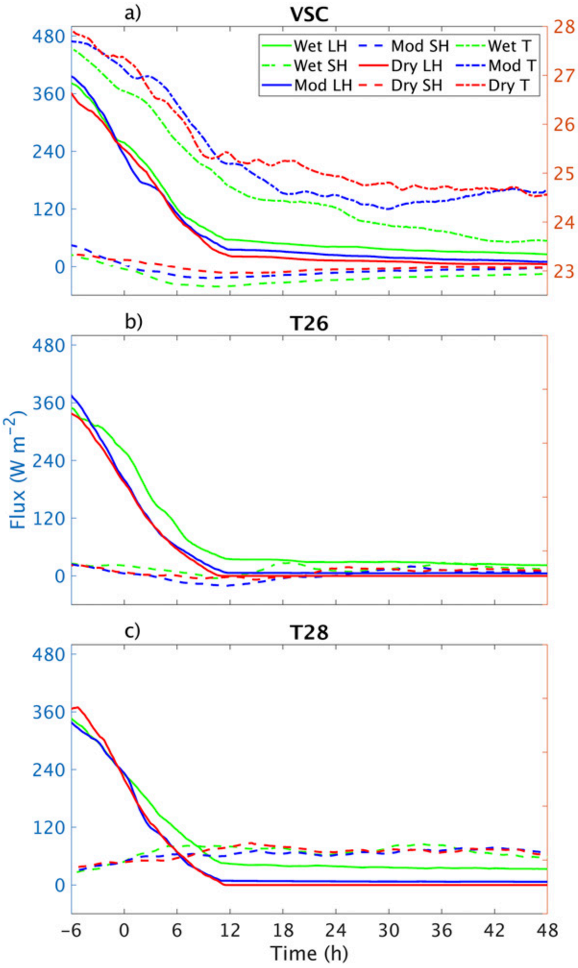

FIG. 15. As in Fig. 13, but for (a) VSC, (b) T26, and (c) T28. Wet, moderate, and dry simulations are shown in green, blue, and red, respectively. Positive (negative) values indicate upward (downward) fluxes. Surface temperature averaged within the same circle is plotted in time for (a), shown in the dashed–dotted plots.

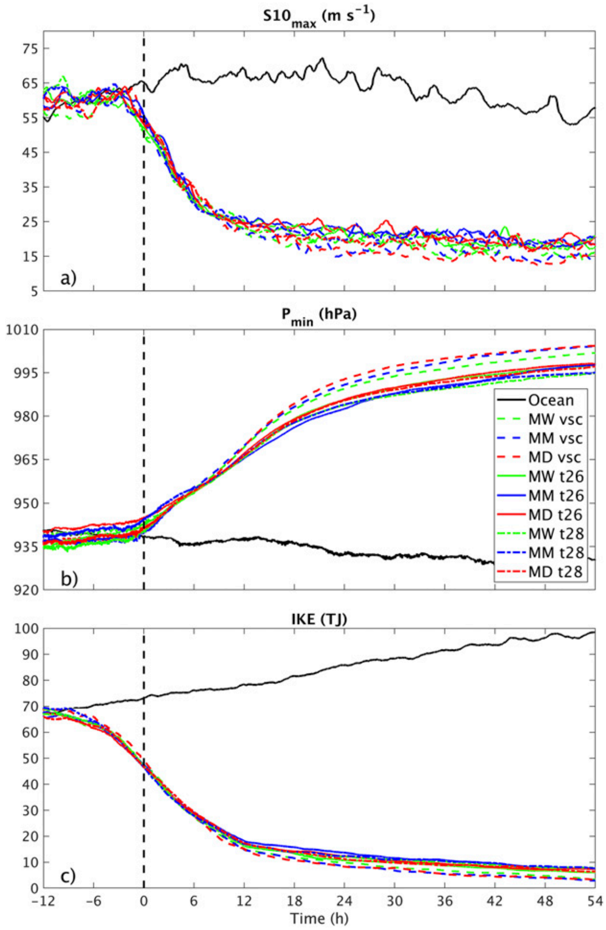

FIG. 16. As in Figs. 5a–c, but for the soil physics sensitivity sets. Plots are moderate Z_0 wet (green), moderate (blue), and dry (red) S_c for VSC (dashed), T26 (solid), and T28 (dashed–dotted).

the first 12 h, as the rougher surfaces caused a faster decay. The maximum winds above the TCBL decayed more slowly.

2) Z_0 and S_c modified the wind decay within different radii and storm-relative quadrants. Higher roughness decelerated the most intense winds more rapidly and briefly accelerated a low-level secondary circulation that ultimately resulted in a flatter radial profile of the 10 m wind speed within a day of landfall. This was more pronounced for increasing Z_0. The effects of Z_0 on the weaker outer-core winds was less pronounced. Conversely, greater S_c slowed the decay of the outer-core winds, while decay rates near the RMW were similar across S_c cases.
3) The sensitivity of the TC intensity to S_c was minimal within 12 h of landfall, when intensities were greater than hurricane strength. Increasing S_c elevated latent heat fluxes across the domain, enhancing midlevel diabatic heating rates and broadening the wind field. However, greater S_c led to cooler surface temperatures through evaporative cooling, resulting in increasingly negative sensible heat fluxes. As the sensible and latent heat fluxes were of comparable magnitude, the net effect was only a slight gain in total enthalpy fluxes for the $S_c = 0.6$ cases, which was not enough to sustain hurricane-force strength. Intensity sensitivity to S_c increased beyond 24 h inland. By this time, TCs had weakened significantly. Additionally, the expansion of the RMW beyond regions of concentrated outer-core lower-tropospheric Q led to conditions supportive of slowing the decay of the wet cases.
4) Additional experiments in which surface temperatures were constant removed the negative feedback of S_c to the sensible heat flux, which allowed TCs to remain slightly stronger inland. Experiments for which soil moisture was permitted to vary in time and in space due to rainfall and evaporation revealed similar intensity trends as in the constant S_c set, as the greater latent heat fluxes were countered by increasingly negative sensible heat fluxes. Intensity differences for this set were similar to the control set, indicating that the negative feedback between soil

moisture and surface temperatures is an important control on inland intensity.

We have found here that a range of realistic Z_0 and S_c values cannot sustain strong TCs. In this way, our results agree with past studies such as T94. However, large-scale saturated soils in high thermal inertia environments may aid in sustaining weaker disturbances, once a significant degree of weakening and RMW expansion has occurred. This latter result corroborates with many of the studies listed in section 1, including Evans et al. (2011). Additionally, T94 and Shen et al. (2002) showed that surface cooling contributes to weakening; however, we advance this idea by analyzing the negative feedback between initial S_c and inland surface temperatures.

Our results apply directly to powerful, mature TCs making landfall at translation speeds that are typical of landfalling TCs in the Atlantic basin. We emphasized sensitivities of the decay to differing large-scale land types. There are many other degrees of freedom we chose not to consider, including weaker intensities at landfall, faster and slower translation speeds, size differences, differences in environmental moisture, wind shear, and lapse rates, and differences in the TC track angle toward land, among many others. It is unfeasible to test every possible permutation. Based on the work of previous studies such as KD95, Wong et al. (2008), Vickery (2005), and Colette et al. (2010), we hypothesize that a faster translation speed would result in further inland penetration of strong winds, and a larger left-to-right decay asymmetry due to the TC motion. Additionally, our finding of a faster decay rate for faster winds suggests that a landfalling TC of a weaker intensity would feature a slower decline in intensity, with a similar decay of the weakest winds. Finally, our findings from section 5 suggest that a weaker TC at landfall featuring a larger RMW would experience heightened sensitivity to S_c sooner. However, these hypotheses require further testing.

Finally, we have not considered other dangerous hazards such as inland flooding and storm surge, which would likely be sensitive to S_c. Regardless, the findings here provide insight toward of the interactions between land surface properties and a powerful landfalling TC, which is crucial for minimizing damages to society.

Acknowledgments. J. Hlywiak was supported by a University of Miami Graduate Fellowship, and both J. Hlywiak and D. Nolan were supported by NSF PREEVENTS Track 2 Award 1663947. We also thank two anonymous reviewers for their helpful and insightful comments.

REFERENCES

Alford, A. A., M. I. Biggerstaff, G. D. Carrie, J. L. Schroeder, B. D. Hirth, and S. M. Waugh, 2019: Near-surface maximum winds during the landfall of Hurricane Harvey. *Geophys. Res. Lett.*, **46**, 973–982, https://doi.org/10.1029/2018GL080013.

——, J. A. Zhang, M. I. Biggerstaff, P. Dodge, F. D. Marks, and D. J. Bodine, 2020: Transition of the hurricane boundary layer during the landfall of Hurricane Irene (2011). *J. Atmos. Sci.*, **77**, 3509–3531, https://doi.org/10.1175/JAS-D-19-0290.1.

Andersen, T. K., and J. M. Shepherd, 2014: A global spatiotemporal analysis of inland tropical cyclone maintenance or intensification. *Int. J. Climatol.*, **34**, 391–402, https://doi.org/10.1002/joc.3693.

Bender, M. A., R. E. Tuleya, and Y. Kurihara, 1987: A numerical study of the effect of island terrain on tropical cyclones. *Mon. Wea. Rev.*, **115**, 130–155, https://doi.org/10.1175/1520-0493(1987)115<0130:ANSOTE>2.0.CO;2.

Bozeman, M. L., D. Niyogi, S. Gopalakrishnan, F. D. Marks, X. Zhang, and V. Tallapragada, 2012: An HWRF-based ensemble assessment of the land surface feedback on the post-landfall intensification of Tropical Storm Fay (2008). *Nat. Hazards*, **63**, 1543–1571, https://doi.org/10.1007/s11069-011-9841-5.

Chen, F., and J. Dudhia, 2001: Coupling an advanced land surface–hydrology model with the Penn State–NCAR MM5 modeling system. Part I: Model implementation and sensitivity. *Mon. Wea. Rev.*, **129**, 569–585, https://doi.org/10.1175/1520-0493(2001)129<0569:CAALSH>2.0.CO;2.

Chen, J., and D. R. Chavas, 2020: The transient responses of an axisymmetric tropical cyclone to instantaneous surface roughening and drying. *J. Atmos. Sci.*, **77**, 2807–2834, https://doi.org/10.1175/JAS-D-19-0320.1.

Chen, Y., and M. K. Yau, 2003: Asymmetric structures in a simulated landfalling hurricane. *J. Atmos. Sci.*, **60**, 2294–2312, https://doi.org/10.1175/1520-0469(2003)060<2294:ASIASL>2.0.CO;2.

Colette, A., N. Leith, V. Daniel, E. Bellone, and D. S. Nolan, 2010: Using mesoscale simulations to train statistical models of tropical cyclone intensity over land. *Mon. Wea. Rev.*, **138**, 2058–2073, https://doi.org/10.1175/2010MWR3079.1.

DeMaria, M., M. Mainelli, L. K. Shay, J. A. Knaff, and J. Kaplan, 2005: Further improvements to the Statistical Hurricane Intensity Prediction Scheme (SHIPS). *Wea. Forecasting*, **20**, 531–543, https://doi.org/10.1175/WAF862.1.

——, J. A. Knaff, and J. Kaplan, 2006: On the decay of tropical cyclone winds crossing narrow landmasses. *J. Appl. Meteor. Climatol.*, **45**, 491–499, https://doi.org/10.1175/JAM2351.1.

Dudhia, J., and Coauthors, 2008: Prediction of Atlantic tropical cyclones with the Advanced Hurricane WRF (AHW) Model. *28th Conf. on Hurricanes and Tropical Meteorology*, Orlando, FL, Amer. Meteor. Soc., 18A.2, https://ams.confex.com/ams/28Hurricanes/techprogram/paper_138004.htm.

Dunion, J. P., 2011: Rewriting the climatology of the tropical North Atlantic and Caribbean Sea atmosphere. *J. Climate*, **24**, 893–908, https://doi.org/10.1175/2010JCLI3496.1.

Eliassen, A., 1971: On the Ekman layer in a circular vortex. *J. Meteor. Soc. Japan*, **49A**, 784–789, https://doi.org/10.2151/jmsj1965.49A.0_784.

Emanuel, K., J. Callaghan, and P. Otto, 2008: A hypothesis for the redevelopment of warm-core cyclones over northern Australia. *Mon. Wea. Rev.*, **136**, 3863–3872, https://doi.org/10.1175/2008MWR2409.1.

Evans, C., R. S. Schumacher, and T. J. Galarneau, 2011: Sensitivity in the overland reintensification of Tropical Cyclone Erin (2007) to near-surface soil moisture characteristics. *Mon. Wea. Rev.*, **139**, 3848–3870, https://doi.org/10.1175/2011MWR3593.1.

——, and Coauthors, 2017: The extratropical transition of tropical cyclones. Part I: Cyclone evolution and direct impacts. *Mon. Wea. Rev.*, **145**, 4317–4344, https://doi.org/10.1175/MWR-D-17-0027.1.

Giammanco, I. M., J. L. Schroeder, and M. D. Powell, 2012: Observed characteristics of tropical cyclone vertical wind profiles. *Wind Struct.*, **15**, 65–86, http://doi.org/10.12989/was.2012.15.1.065.

Hong, S. Y., Y. Noh, and J. Dudhia, 2006: A new vertical diffusion package with an explicit treatment of entrainment processes.

Mon. Wea. Rev., **134**, 2318–2341, https://doi.org/10.1175/MWR3199.1.

Janjić, Z., 2002: Nonsingular implementation of the Mellor-Yamada level 2.5 scheme in the NCEP Meso model. NCEP Office Note 437, 61 pp., http://www.emc.ncep.noaa.gov/officenotes/newernotes/on437.pdf.

Jordan, C. L., 1958: Mean soundings for the West Indies area. *J. Atmos. Sci.*, **15**, 91–97, https://doi.org/10.1175/1520-0469(1958)015<0091:MSFTWI>2.0.CO;2.

Kaplan, J., and M. DeMaria, 1995: A simple empirical model for predicting the decay of tropical cyclone winds after landfall. *J. Appl. Meteor. Climatol.*, **34**, 2499–2512, https://doi.org/10.1175/1520-0450(1995)034<2499:ASEMFP>2.0.CO;2.

——, and ——, 2001: On the decay of tropical cyclone winds after landfall in the New England area. *J. Appl. Meteor.*, **40**, 280–286, https://doi.org/10.1175/1520-0450(2001)040<0280:OTDOTC>2.0.CO;2.

Kellner, O., D. Niyogi, M. Lei, and A. Kumar, 2012: The role of anomalous soil moisture on the inland reintensification of Tropical Storm Erin (2007). *Nat. Hazards*, **63**, 1573–1600, https://doi.org/10.1007/s11069-011-9966-6.

Kepert, J. D., J. Schwendike, and H. Ramsay, 2016: Why is the tropical cyclone boundary layer not ''well mixed''? *J. Atmos. Sci.*, **73**, 957–973, https://doi.org/10.1175/JAS-D-15-0216.1.

Kilroy, G., R. K. Smith, and M. T. Montgomery, 2016a: Why do model tropical cyclones grow progressively in size and decay in intensity after reaching maturity? *J. Atmos. Sci.*, **73**, 487–503, https://doi.org/10.1175/JAS-D-15-0157.1.

——, ——, ——, B. Lynch, and C. Earl-Spurr, 2016b: A case-study of a monsoon low that formed over the sea and intensified over land as seen in ECMWF analyses. *Quart. J. Roy. Meteor. Soc.*, **142**, 2244–2255, https://doi.org/10.1002/qj.2814.

Kishtawal, C. M., D. Niyogi, A. Kumar, M. L. Bozeman, and O. Kellner, 2012: Sensitivity of inland decay of North Atlantic tropical cyclones to soil parameters. *Nat. Hazards*, **63**, 1527–1542, https://doi.org/10.1007/s11069-011-0015-2.

Knupp, K. R., J. Walters, and M. Biggerstaff, 2006: Doppler profiler and radar observations of boundary layer variability during the landfall of Tropical Storm Gabrielle. *J. Atmos. Sci.*, **63**, 234–251, https://doi.org/10.1175/JAS3608.1.

Kosiba, K. A., and J. Wurman, 2014: Finescale dual-Doppler analysis of hurricane boundary layer structures in Hurricane Frances (2004) at landfall. *Mon. Wea. Rev.*, **142**, 1874–1891, https://doi.org/10.1175/MWR-D-13-00178.1.

Kossin, J. P., 2018: A global slowdown of tropical-cyclone translation speed. *Nature*, **558**, 104–107, https://doi.org/10.1038/s41586-018-0158-3.

Krupar, R. J., J. L. Schroeder, D. A. Smith, S. L. Kang, and S. Lorsolo, 2016: A comparison of ASOS near-surface winds and WSR-88D-derived wind speed profiles measured in landfalling tropical cyclones. *Wea. Forecasting*, **31**, 1343–1361, https://doi.org/10.1175/WAF-D-15-0162.1.

Leroux, M.-D., and Coauthors, 2018: Recent advances in research and forecasting of tropical cyclone track, intensity, and structure at landfall. *Trop. Cyclone Res. Rev.*, **7**, 85–105, https://doi.org/10.6057/2018TCRR02.02.

Lim, J. O. J., and S. Y. Hong, 2005: Effects of bulk ice microphysics on the simulated monsoonal precipitation over East Asia. *J. Geophys. Res.*, **110**, D24201, https://doi.org/10.1029/2005JD006166.

Marks, F. D., and Coauthors, 1998: Landfalling tropical cyclones: Forecast problems and associated research opportunities. *Bull. Amer. Meteor. Soc.*, **79**, 305–323, https://doi.org/10.1175/1520-0477(1998)079<0305:LTCFPA>2.0.CO;2.

Masters, F. J., H. W. Tieleman, and J. A. Balderrama, 2010: Surface wind measurements in three Gulf Coast hurricanes of 2005. *J. Wind Eng. Ind. Aerodyn.*, **98**, 533–547, https://doi.org/10.1016/j.jweia.2010.04.003.

Miller, B. I., 1964: A study of the filling of Hurricane Donna (1960) over land. *Mon. Wea. Rev.*, **92**, 389–406, https://doi.org/10.1175/1520-0493(1964)092<0389:ASOTFO>2.3.CO;2.

Montgomery, M. T., H. D. Snell, and Z. Yang, 2001: Axisymmetric spindown dynamics of hurricane-like vortices. *J. Atmos. Sci.*, **58**, 421–435, https://doi.org/10.1175/1520-0469(2001)058<0421:ASDOHL>2.0.CO;2.

——, N. Van Sang, R. K. Smith, and J. Persing, 2009: Do tropical cyclones intensify by WISHE? *Quart. J. Roy. Meteor. Soc.*, **135**, 1697–1714, https://doi.org/10.1002/qj.459.

Nguyen, L. T., J. Molinari, and D. Thomas, 2014: Evaluation of tropical cyclone center identification methods in numerical models. *Mon. Wea. Rev.*, **142**, 4326–4339, https://doi.org/10.1175/MWR-D-14-00044.1.

Nolan, D. S., 2011: Evaluating environmental favorableness for tropical cyclone development with the method of point-downscaling. *J. Adv. Model. Earth Syst.*, **3**, M08001, https://doi.org/10.1029/2011MS000063.

Onderlinde, M. J., and D. S. Nolan, 2017: The tropical cyclone response to changing wind shear using the method of time-varying point-downscaling. *J. Adv. Model. Earth Syst.*, **9**, 908–931, https://doi.org/10.1002/2016MS000796.

Ooyama, K., 1969: Numerical simulation of the life cycle of tropical cyclones. *J. Atmos. Sci.*, **26**, 3–40, https://doi.org/10.1175/1520-0469(1969)026<0003:NSOTLC>2.0.CO;2.

Pollard, R. T., P. B. Rhines, and R. O. Thompson, 1972: The deepening of the wind-mixed layer. *Geophys. Astrophys. Fluid Dyn.*, **4**, 381–404, https://doi.org/10.1080/03091927208236105.

Powell, M. D., and T. A. Reinhold, 2007: Tropical cyclone destructive potential by integrated kinetic energy. *Bull. Amer. Meteor. Soc.*, **88**, 513–526, https://doi.org/10.1175/BAMS-88-4-513.

——, P. J. Vickery, and T. A. Reinhold, 2003: Reduced drag coefficient for high wind speeds in tropical cyclones. *Nature*, **422**, 279–283, https://doi.org/10.1038/nature01481.

Schubert, W. H., and J. H. Hack, 1982: Inertial stability and tropical cyclone development. *J. Atmos. Sci.*, **39**, 1687–1697, https://doi.org/10.1175/1520-0469(1982)039<1687:ISATCD>2.0.CO;2.

Shen, W., I. Ginis, and R. E. Tuleya, 2002: A numerical investigation of land surface water on landfalling hurricanes. *J. Atmos. Sci.*, **59**, 789–802, https://doi.org/10.1175/1520-0469(2002)059<0789:ANIOLS>2.0.CO;2.

Smith, R. K., and M. T. Montgomery, 2010: Hurricane boundary-layer theory. *Quart. J. Roy. Meteor. Soc.*, **136**, 1665–1670, https://doi.org/10.1002/qj.679.

Tang, S., R. K. Smith, M. T. Montgomery, and M. Gu, 2016: Numerical study of the spin-up of a tropical low over land during the Australian monsoon. *Quart. J. Roy. Meteor. Soc.*, **142**, 2021–2032, https://doi.org/10.1002/qj.2797.

Tuleya, R. E., 1994: Tropical storm development and decay: Sensitivity to surface boundary conditions. *Mon. Wea. Rev.*, **122**, 291–304, https://doi.org/10.1175/1520-0493(1994)122<0291:TSDADS>2.0.CO;2.

Vickery, P. J., 2005: Simple empirical models for estimating the increase in the central pressure of tropical cyclones after landfall along the coastline of the United States. *J. Appl. Meteor.*, **44**, 1807–1826, https://doi.org/10.1175/JAM2310.1.

Vigh, J. L., and W. H. Schubert, 2009: Rapid development of the tropical cyclone warm core. *J. Atmos. Sci.*, **66**, 3335–3350, https://doi.org/10.1175/2009JAS3092.1.

Wierenga, J., 1993: Representative roughness parameters for homogeneous terrain. *Bound.-Layer Meteor.*, **63**, 323–363, https://doi.org/10.1007/BF00705357.

Williams, G. J., 2019: Idealized simulations of the inner core boundary layer structure in a landfalling tropical cyclone. Part I: Kinematic structure. *Trop. Cyclone Res. Rev.*, **8**, 47–67, https://doi.org/10.1016/j.tcrr.2019.07.006.

Wong, M. L., J. C. Chan, and W. Zhou, 2008: A simple empirical model for estimating the intensity change of tropical cyclones after landfall along the south China coast. *J. Appl. Meteor. Climatol.*, **47**, 326–338, https://doi.org/10.1175/2007JAMC1633.1.

Wu, C. C., H. J. Cheng, Y. Wang, and K. H. Chou, 2009: A numerical investigation of the eyewall evolution in a landfalling typhoon. *Mon. Wea. Rev.*, **137**, 21–40, https://doi.org/10.1175/2008MWR2516.1.

Yablonsky, R. M., and I. Ginis, 2009: Limitation of one-dimensional ocean models for coupled hurricane–ocean model forecasts. *Mon. Wea. Rev.*, **137**, 4410–4419, https://doi.org/10.1175/2009MWR2863.1.

Yang, M. J., S. A. Braun, and D. S. Chen, 2011: Water budget of Typhoon Nari (2001). *Mon. Wea. Rev.*, **139**, 3809–3828, https://doi.org/10.1175/MWR-D-10-05090.1.

Zhang, C., Y. Wang, and K. Hamilton, 2011: Improved representation of boundary layer clouds over the southeast pacific in ARW-WRF using a modified Tiedtke cumulus parameterization scheme. *Mon. Wea. Rev.*, **139**, 3489–3513, https://doi.org/10.1175/MWR-D-10-05091.1.

Zhang, F., and Z. Pu, 2017: Effects of vertical eddy diffusivity parameterization on the evolution of landfalling hurricanes. *J. Atmos. Sci.*, **74**, 1879–1905, https://doi.org/10.1175/JAS-D-16-0214.1.

Zhang, J. A., R. F. Rogers, D. S. Nolan, and F. D. Marks, 2011a: On the characteristic height scales of the hurricane boundary layer. *Mon. Wea. Rev.*, **139**, 2523–2535, https://doi.org/10.1175/MWR-D-10-05017.1.

——, P. Zhu, F. J. Masters, R. F. Rogers, and F. D. Marks, 2011b: On momentum transport and dissipative heating during hurricane landfalls. *J. Atmos. Sci.*, **68**, 1397–1404, https://doi.org/10.1175/JAS-D-10-05018.1.